Thermal and viscous boundary layers in turbulent Rayleigh–Bénard convection

J. D. Scheel[1]**†, E. Kim**[1] **and K. R. White**[2]

[1] Department of Physics, Occidental College, 1600 Campus Road, M21, Los Angeles, CA 90041, USA

[2] Department of Applied Mathematics and Statistics, University of California Santa Cruz, Mail Stop SOE GRADS, 1156 High Street, Santa Cruz, CA 95064, USA

We present the results from numerical simulations of turbulent Rayleigh–Bénard convection for an aspect ratio (diameter/height) of 1.0, Prandtl numbers of 0.4 and 0.7, and Rayleigh numbers from 1×10^5 to 1×10^9. Detailed measurements of the thermal and viscous boundary layer profiles are made and compared to experimental and theoretical (Prandtl–Blasius) results. We find that the thermal boundary layer profiles disagree by more than 10 % when scaled with the similarity variable (boundary layer thickness) and likewise disagree with the Prandtl–Blasius results. In contrast, the viscous boundary profiles collapse well and do agree (within 10 %) with the Prandtl–Blasius profile, but with worsening agreement as the Rayleigh number increases. We have also investigated the scaling of the boundary layer thicknesses with Rayleigh number, and again compare to experiments and theory. We find that the scaling laws are very robust with respect to method of analysis and they mostly agree with the Grossmann–Lohse predictions coupled with laminar boundary layer theory within our numerical uncertainty.

Key words: Bénard convection, boundary layer structure, turbulent convection

1. Introduction

Turbulent convection is an important area of study that has applications to diverse phenomena such as that which takes place in heat exchangers in power plants and melting processes, as well as natural convection in the Earth's atmosphere, core and oceans, and in the Sun and Jupiter.

In Rayleigh–Beńard (RB) convection, a fluid cell is bounded by horizontal parallel plates and kept at a constant temperature difference ΔT. The dimensionless Rayleigh number, Ra, is proportional to ΔT. As the Rayleigh number increases past a critical value, a buoyancy-driven instability causes the conducting state to bifurcate to a convection state consisting of straight, parallel rolls. Then if the Rayleigh number is increased further, these states can bifurcate to spatiotemporal chaotic states. When the Rayleigh number becomes very large, this system becomes fully turbulent. This fully turbulent system is very complex and bears little resemblance to the weakly turbulent system, which is chaotic but still retains a clear and coherent underlying roll structure.

† Email address for correspondence: jscheel@oxy.edu

The results of experiments (Qiu & Xia 1998; Sreenivasan, Bershadskii & Niemela 2002; Funfschilling & Ahlers 2004; Brown, Nikolaenko & Ahlers 2005; Zhou, Sun & Xia 2007) and direct numerical simulations (Verzicco & Camussi 2003; Chandra & Verma 2011; Wagner, Shishkina & Wagner 2012) have found thermal plumes at these large Rayleigh numbers and shown the presence of a large-scale circulation (LSC) throughout the entire cell, which carries the plumes in a circular manner. The plane of the circulation is vertical, but its orientation in a cylindrical cell is arbitrary and changes with time, as does the strength of the circulation. In addition, there are thin, thermal and viscous boundary layers on the bottom and top of the cell, and it is not well understood how the boundary layers interact with the LSC.

In this paper we perform three-dimensional numerical simulations of the Boussinesq equations for no-slip boundary conditions, for an aspect ratio of 1.0, Rayleigh numbers between 1×10^5 and 1×10^9, and Prandtl numbers of 0.4 and 0.7. We used the cases with a Prandtl number of 0.7 to compare to many experiments (Castaing *et al.* 1989; Wu & Libchaber 1992; Chavanne *et al.* 1997; Niemela *et al.* 2000; Ahlers *et al.* 2009*a*; Burnishev, Segre & Steinberg 2010; du Puits, Resagk & Thess 2010; Urban, Musilova & Skrbek 2011). We used the cases with a Prandtl number of 0.4 to observe the LSC and any possible cessations, since the LSC is stronger and cessations more likely for a lower Prandtl number at any given Rayleigh number (Breuer *et al.* 2004). In this paper, we focus on the boundary layers, which are the key to understanding the nature of the turbulence in RB convection.

Boundary layer profiles and thicknesses have been measured both experimentally and numerically, and there is some disagreement as to both the shape of the profiles and the scaling of boundary layer thickness with Rayleigh number. A comparison of boundary layer results is given in table 1. For a more comprehensive review, see Ahlers, Grossmann & Lohse (2009*b*). The shape of the boundary layers is important, because it can provide insight into whether or not the boundary layers are laminar or turbulent, and also predict if and when the boundary layer may become turbulent as the 'ultimate regime' is reached (Funfschilling, Bodenschatz & Ahlers 2009; He *et al.* 2012). Theoretically, if the boundary layers are laminar, they should exhibit self-similarity (van Reeuwijk *et al.* 2008) and possibly take a Prandtl–Blasius shape (Schlichting & Gersten 2000). The Prandtl–Blasius theory assumes that there is a constant horizontal velocity just above the boundary layer, as is true if there is a constant LSC.

A comparison of scaling results is also shown in table 1 as well as later in table 7. Theoretically, it is expected that the thermal boundary layer thickness should be inversely related to the scaling of the Nusselt number with Rayleigh number. Likewise, the viscous boundary layer thickness should be inversely related to the square root of the scaling of Reynolds number with Rayleigh number (Schlichting & Gersten 2000).

The rest of the paper is organized as follows. First, we describe the numerical simulations, including extensive convergence tests. Next, we discuss the scaling of Nusselt number with Rayleigh number, and of Reynolds number with Rayleigh number, and compare to other results. Finally, we look at the boundary layers, both in profile and in terms of their scaling with Rayleigh number.

2. Boussinesq equations

The system is modelled by the Boussinesq equations (Chandrasekhar 1961). The variables are non-dimensionalized by specifying the length in terms of the cell height d, the temperature in terms of ΔT, and the time in units of the vertical

Group	Type	Range of Ra	σ	Collapse well	Agree with PB	β_θ	β_v
Current work	λ_θ	10^5–10^9	0.7, 0.4	No	No	-0.25 ± 0.01	—
Stevens, Verzicco & Lohse (2010)* and Stevens et al. (2012)*	λ_θ	10^8–10^{12}	0.7	Yes	No	-0.29	-0.28
Shi, Emran & Schumacher (2012)*	$\lambda_\theta, \lambda_v$	10^9–10^{10}	0.7	—	No	—	—
Zhou et al. (2010, 2011)*	$\lambda_\theta, \lambda_v$	10^8–10^{11}	0.7	—	Yes	—	—
du Puits, Resagk & Thess (2012)	λ_θ	10^9–10^{10}	0.7	Yes	No	—	—
Shishkina & Thess (2009)*	λ_θ	10^8–10^9	4.38	Yes	No	—	—
Lui & Xia (1998)	λ_θ	10^8–10^{10}	≈ 7	No	—	-0.285 ± 0.04	—
Current work	λ_v	10^5–10^9	0.7, 0.4	Yes	Yes	—	-0.18 ± 0.01
Zhou & Xia (2010)	λ_v	10^9–10^{11}	4.3	Yes	Yes	—	—
du Puits, Resagk & Thess (2007a, 2009)	λ_v	10^9–10^{12}	0.7	Yes	No	-0.2540	—
van Reeuwijk, Jonker & Hanjalic (2008)*	λ_v	10^5–10^8	1	Yes	—	-0.27	-0.13
Sun, Cheung & Xia (2008)	λ_v	10^9–10^{10}	4.3	Yes	—	-0.33 ± 0.05	-0.27 ± 0.01
Lam et al. (2002)	λ_v	10^8–10^{10}	6–1027	Yes	—	(−)	-0.16 ± 0.02
Xin, Xia & Tong (1996)	λ_v	10^8–10^{10}	≈ 7	Yes	—	-0.29	-0.16 ± 0.02

TABLE 1. Comparison of results for thermal (λ_θ) and viscous (λ_v) boundary layer profiles. Some groups found that their boundary layer profiles collapsed well when the z axis was scaled by the boundary layer thickness. Others found the opposite. Likewise, some groups found that their profiles agreed well with the theoretical Prandtl–Blasius (PB) profile and others found the opposite. If not clearly stated by the authors, we define 'collapse well' or 'agree with PB' as agreeing within 10 % for the entire range of Rayleigh numbers given. We also include the scaling exponents (when reported) β_θ and β_v as defined in (3.5) and (3.6). A dash indicates that an analysis was not performed or such data were not discussed in the paper. The asterisk * indicates numerical simulations; the others are experiments.

thermal diffusion time $\tau_v = d^2/\kappa$, where κ is the thermal diffusivity. The equations are

$$\sigma^{-1}(\partial_t + \boldsymbol{u} \cdot \boldsymbol{\nabla})\boldsymbol{u} = -\boldsymbol{\nabla}P + \nabla^2\boldsymbol{u} + Ra\,\theta\boldsymbol{z}, \qquad (2.1)$$

$$(\partial_t + \boldsymbol{u} \cdot \boldsymbol{\nabla})\theta = \nabla^2\theta, \qquad (2.2)$$

$$\boldsymbol{\nabla} \cdot \boldsymbol{u} = 0. \qquad (2.3)$$

The variable $\boldsymbol{u}(\boldsymbol{r}, t) \equiv (u, v, w)$ is the velocity field, $P(\boldsymbol{r}, t)$ is the pressure and $\theta(\boldsymbol{r}, t)$ is the temperature field. The symbol ∂_t indicates time differentiation, and $\boldsymbol{z}$ is a unit vector in the vertical direction. The Prandtl number (σ) is ν/κ, where ν is the kinematic viscosity. The Rayleigh number (Ra) is $\alpha g \Delta T d^3/\kappa\nu$, where α is the thermal expansion coefficient and g is the acceleration of gravity. The aspect ratio (Γ) is defined for cylindrical cells as the ratio of the diameter to the height.

Our boundary conditions along the top and bottom plates are no-slip and conducting:

$$\boldsymbol{u} = 0 \quad \text{at } z = 0, 1, \quad \theta = 1 \quad \text{at } z = 0, \quad \theta = 0 \quad \text{at } z = 1. \qquad (2.4)$$

For realistic boundary conditions on the sidewalls, we use no-slip velocity boundary conditions and insulating thermal boundaries:

$$\boldsymbol{u} = 0, \quad \frac{\partial\theta}{\partial r} = 0 \quad \text{at } r = \Gamma. \qquad (2.5)$$

For all our runs and calculations, we used a cylindrical cell of aspect ratio $\Gamma = 1.0$.

To solve the Boussinesq equations with rotation, we used the code Nek5000 (Fischer, Lottes & Kerkemeier 2008), a parallel, spectral element code developed to solve the Navier–Stokes equation. This code is now readily available and is used by more than two dozen research institutions.

2.1. *Convergence tests*

It is very important to have a convergent, well-resolved code in turbulent Rayleigh–Bénard convection to make sure that the experiments are accurately modelled by the simulations (Shishkina *et al.* 2010; Stevens *et al.* 2010).

We will use Nusselt number as a globally averaged quantity to assess convergence as well as to compare our data with other simulations and experiments. The Nusselt number is defined as the ratio of the total heat transported across the cell in the z direction divided by the heat transported via conduction only. For our numerical simulations, we compute the Nusselt number (Nu) by finding the heat transported out of the cell:

$$Nu = \frac{\displaystyle\int \boldsymbol{\nabla}T \cdot \mathrm{d}\boldsymbol{A}}{\displaystyle\int \hat{n} \cdot \mathrm{d}\boldsymbol{A}}, \qquad (2.6)$$

where $\mathrm{d}\boldsymbol{A}$ is an area element of the top surface whose normal is parallel to the direction of heat transport $\hat{n}$.

For purposes of comparison to other numerical simulations, $\tau_v = \sqrt{\sigma Ra}\,\tau$, where τ is the dimensionless time used by other groups (Shishkina & Thess 2009; Stevens *et al.* 2010; Shi *et al.* 2012) and τ_v is the dimensionless time we use in our simulations. We ran our simulations for at least $0.01\,\tau_v$, and did not start computing important quantities (Nusselt number, Reynolds number, boundary layer thicknesses, etc.) until after the system settled into the turbulent state. Then we ran out our

Spat. resol.	dt	Nu	λ_θ^{sl}	$\delta\lambda_\theta^{sl}$ (%)	λ_v^{sl}	$\delta\lambda_v^{sl}$ (%)	Total time
9	1×10^{-7}	19.56	0.0271	3.8	0.0181	9.9	0.027
11	1×10^{-7}	19.44	0.0272	1.4	0.0179	8.1	0.049
13	1×10^{-7}	19.39	0.0261	3.9	0.0174	6.4	0.024
15	1×10^{-7}	19.70	0.0275	2.2	0.0184	8.2	0.022
11	4×10^{-7}	19.41	0.0262	1.5	0.0178	7.3	0.023
11	1×10^{-7}	19.44	0.0272	1.4	0.0179	8.0	0.049
11	5×10^{-8}	19.71	0.0275	5.1	0.0185	7.0	0.020
11	1×10^{-8}	19.14	0.0283	12.0	0.0198	12.0	0.023

TABLE 2. Demonstration of convergence for $\sigma = 0.4$, $\Gamma = 1$ and $Ra = 2 \times 10^7$. The spatial resolution is the number of interpolation points in each dimension. The time step dt is noted. Also, in this case, 840 elements were used. The Nusselt number Nu is given in the third column, and the thermal λ_θ^{sl} and viscous λ_v^{sl} boundary layer thicknesses are also given (as computed from the slope method for a 50 % cut as discussed in the text). Note that the relative size of the fluctuations in the boundary layer thickness are also given as $\delta\lambda_\theta^{sl}$ and $\delta\lambda_v^{sl}$ (as percentages). The total time is the simulation time in units of thermal diffusion times, and note here that one turnover time is 0.0012 thermal diffusion times.

simulations for at least $0.04\,\tau_v$, but often much longer. Roughly this translates into waiting ~ 6 turnover times for transients to settle, and then using at least 30 turnover times (but often more than 100) for our averages. A turnover time in our case is defined as σ/Re, approximately the time it takes a fluid element to traverse the cell in the vertical direction.

We studied our convergence in more detail, by varying our time step dt, while keeping our resolution N fixed. The variable N refers to the number of Gauss–Lobatto–Legendre (GLL) interpolation points in each dimension. Since the code is spectral, the points are not equally spaced, but are more closely spaced near the boundaries, exactly where more resolution is required. We also kept our dt fixed and then varied our N. The results are shown in table 2. Note for the convergence cases that we only ran out for about 20 turnover times, as can be seen by the last column in table 2. We see that the Nusselt numbers are well converged for all N and dt used. For our production runs, we typically used an N of 11 and the smallest dt required to satisfy our Courant–Friedrichs–Levy condition (<1).

By looking at table 2, we see that our Nusselt number varies by at most 3 % (also roughly true for the standard deviation in our Nusselt number time series). As can be seen in figure 1, our results agree very well with other numerical simulations (Stevens *et al.* 2010) and experiments (Ahlers *et al.* 2009*a*).

We also compare our resolution to the Kolmogorov scale as defined by Stevens *et al.* (2010):

$$\eta = d \left(\frac{\sigma^2}{Ra\,Nu} \right)^{1/4}. \tag{2.7}$$

In table 3 we compare our maximum grid resolution l to η, and find that the maximum grid resolution is either smaller than or comparable to the Kolmogorov scale. The case with a Rayleigh number of 5×10^7 is the least well-resolved, but even that data point falls very well on most of our data plots, suggesting that this is the poorest resolution tolerated by our simulations of turbulent RB convection. We also computed
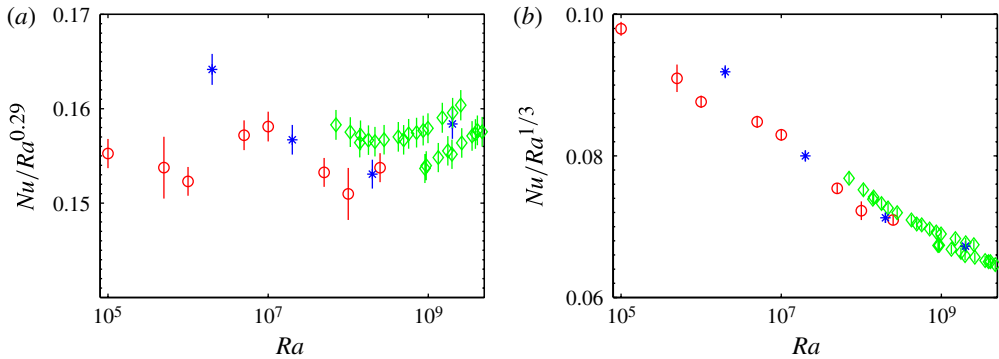
FIGURE 1. (Colour online) (*a*) Comparison of Nusselt numbers between this paper (∘),
Stevens *et al.* (2010) (∗) and Ahlers *et al.* (2009*a*) (⋄) for $\sigma = 0.7$. Note that $\Gamma = 0.5$ for
both Ahlers *et al.* (2009*a*) and Stevens *et al.* (2010), in contrast to our $\Gamma = 1.0$. Nonetheless,
there is excellent agreement, suggesting that our simulations are well-converged. Also note
that we computed our error bars by the same method as in Stevens *et al.* (2010). (*b*) The same
plot, except that the Grossmann–Lohse predicted scaling exponent of $1/3$ is used instead
of 0.29.

Ra	Nu	N_{bl}	l/η
1×10^5	4.38	20	0.28
5×10^5	6.91	16	0.47
1×10^6	8.37	14	0.58
5×10^6	13.78	13	0.99
1×10^7	16.94	13	1.24
5×10^7	26.19	12	2.07
1×10^8	31.54	20	1.27
2.5×10^8	41.95	16	1.74

TABLE 3. Demonstration of convergence, based on number of data points in the boundary
layer (N_{bl}) and the maximum grid scale l compared with the Kolmogorov scale η. The data
here are for $\sigma = 0.7$ and $\Gamma = 1$.

the number of grid points in the thermal boundary layer N_{bl}, since we did increase our
resolution there in order to resolve the boundary layers more properly. The quantity
N_{bl} is computed by taking the thermal boundary layer thickness (λ_θ) and dividing
by the resolution in the boundary layer. Again, we find that the boundary layers are
adequately resolved. Also, the requirement on the number of nodes in the thermal and
kinetic boundary layers according to Shishkina *et al.* (2010) is more than adequately
satisfied.

   If we compare the boundary layer thicknesses (see § 3.3 for a description of how the
boundary layer thicknesses were measured) in table 2, we do see results that vary by
2 % for λ_θ^{sl} and 5 % for λ_v^{sl} when the spatial resolution is varied, and 7 % for λ_θ^{sl} and
8 % for λ_v^{sl} when the time step is varied. This is more than the variation in Nusselt
number, and this is perhaps not so surprising since boundary layer thicknesses are
less of a globally averaged quantity than Nusselt number. Also, the boundary layer
thicknesses vary quite a bit with time, and we give the size of the relative fluctuations

Averaging time	$\langle\lambda_\theta^{sl}\rangle$	$\langle\lambda_v^{sl}\rangle$	S_θ	S_v
0.005	0.0134	0.0091	2.1651	2.3203
0.010	0.0136	0.0092	2.1568	2.3327
0.015	0.0137	0.0093	2.1591	2.3393
0.020	0.0136	0.0092	2.1693	2.3492
0.025	0.0135	0.0092	2.1814	2.3490
0.030	0.0134	0.0092	2.1815	2.3460
0.035	0.0134	0.0092	2.1835	2.3442
0.040	0.0133	0.0092	2.1753	2.3451
0.045	0.0133	0.0092	2.1777	2.3474
0.050	0.0133	0.0092	2.1867	2.3530
0.054	0.0133	0.0092	2.1958	2.3568

TABLE 4. Tests of simulation time. Various quantities are computed for different simulation times and for a 10 % cut. One turnover time is 0.0005 thermal diffusion times for this case of $\sigma = 0.4$ and $Ra = 2 \times 10^8$. See §3.3 for a description of how $\langle\lambda_\theta^{sl}\rangle$ and $\langle\lambda_v^{sl}\rangle$ were measured. See (3.16) and below for definitions of S_v and S_θ.

in table 2 to highlight this. The quantity $\delta\lambda_\theta^{sl}$ is given by the standard deviation in λ_θ^{sl} for our time series, divided by the average value for λ_θ^{sl} (and then times 100 to get a percentage). The same value is computed for our viscous boundary thicknesses as well. This information is useful, since it gives us a sense of the variation in boundary layer thicknesses and our uncertainty in these quantities. Also, note that the variation for our smallest dt (1×10^{-8}) is the largest, suggesting that there were some fairly large fluctuations in the boundary layer for this particular case, which would have benefited from being run for a longer time.

Finally, we have studied whether or not the averaging time has an effect on the results as shown in table 4. We find that as long as we average for at least 10 turnover times, the boundary layer thicknesses vary by at most 3 %. The shape factors also vary by at most 2 %, but there is a slight trend towards higher values, suggesting that longer averaging times help for these values. There is more uncertainty in shape factors partially because this quantity is calculated from the boundary layer profile, so any error is compounded when computing the integrals in (3.15) and (3.14). An upper bound of varying by at most 3 % encompasses the uncertainty due to averaging time for both boundary layer thicknesses and shape factors.

As a result of our uncertainty analysis and convergence testing, we define the term 'collapse well' to be a variation of less than 10 % and vice versa.

3. Results

3.1. *Scaling of Nusselt number with Rayleigh number*

We investigated how the Nusselt number scales with Rayleigh number, as shown in figure 2, since this scaling suggests different methods of heat transport. The scaling equation is given as

$$Nu = Nu_0 Ra^{\gamma_{Nu}}. \tag{3.1}$$

There is also a scaling dependence with Prandtl number, but we did not vary our Prandtl number enough for this to be determined, as can be seen in figure 2. Recent results for Nusselt number scaling with Rayleigh number show good agreement, at least for Rayleigh numbers less than 1×10^{11}, as can be seen in table 5. For simplicity,
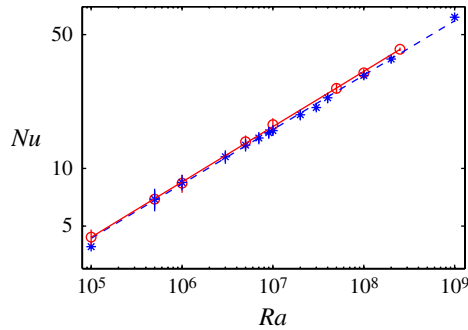
FIGURE 2. (Colour online) Nusselt number versus Rayleigh number for $\sigma = 0.7$ (solid line, $\circ$) and $\sigma = 0.4$ (dashed line, $*$). The slopes are 0.29 ± 0.01 for $\sigma = 0.7$ and 0.284 ± 0.005 for $\sigma = 0.4$. The data point for $Ra = 1 \times 10^5$ was not included in the fits since it was an outlier.

Group	Range of Ra	σ	Γ	Nu_0	γ_{Nu}
Current work	10^5–10^8	0.7	1	0.16 ± 0.04	0.29 ± 0.01
Current work	10^5–10^9	0.4	1	0.16 ± 0.02	0.284 ± 0.005
Urban *et al.* (2011)	10^7–10^9	0.7	1	0.156	2/7
Bailon-Cuba, Emran & Schumacher (2010)*	10^7–10^9	0.7	1	0.145	0.294
Kerr (2001)*	10^6–10^8	0.7	1	—	0.27 ± 0.02
Belmonte *et al.* (1994)	10^7–10^{11}	0.7	1	0.18	0.29
Wu & Libchaber (1992)	10^6–10^{10}	0.7	1	0.217	0.285
Wagner *et al.* (2012)*	10^4–10^9	0.8	1	—	0.298
Burnishev *et al.* (2010)	10^8–10^{12}	0.8	1	0.12 ± 0.01	0.304 ± 0.005
Stevens *et al.* (2010)*	10^6–10^{11}	0.7	1/2	0.12	0.30
Ahlers *et al.* (2009a)	10^8–10^{11}	0.67	1/2	0.13	0.30
Niemela *et al.* (2000)	10^6–10^{17}	$\simeq 0.7$	1/2	0.12	0.309
Benzi, Toschi & Tripiccione (1998)*	10^6–10^8	1	1	—	0.283 ± 0.003
Chavanne *et al.* (1997)	10^7–10^{11}	0.66–0.73	1/2	—	2/7
Castaing *et al.* (1989)	10^7–10^{11}	0.64–1.14	1	0.23	0.282

TABLE 5. Comparison of Nusselt number scaling as given by (3.1). The asterisk * indicates numerical simulations; the others are experiments.

we have presented data for Prandtl numbers and aspect ratios similar to ours. For a more comprehensive review, see Ahlers *et al.* (2009b).

Note that our scaling results agree best with experiments in exactly the same range and parameters, including Belmonte, Tilgner & Libchaber (1994) and Urban *et al.* (2011), suggesting that our simulations are well-converged and we are running the simulations for the appropriate amount of time.

We determined our numerical uncertainties here by first computing instantaneous quantities, such as the Nusselt number. Our Nusselt number for a particular Rayleigh number is given by the long time average, and the uncertainty is the standard deviation. Then, when performing a fit to determine scaling parameters, we propagated that uncertainty.
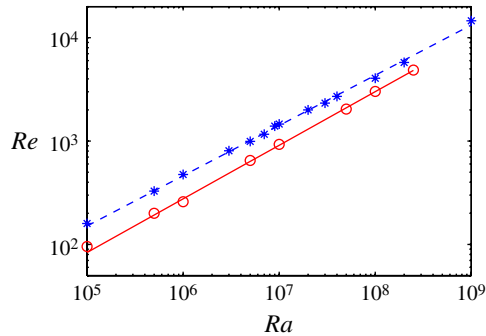
FIGURE 3. (Colour online) Reynolds number versus Rayleigh number for $\sigma = 0.7$ (solid line, ○) and $\sigma = 0.4$ (dashed line, ∗). The slopes are 0.518 ± 0.001 for $\sigma = 0.7$ and 0.486 ± 0.001 for $\sigma = 0.4$. Note in this case that the error bars are smaller than the marker size.

Group	Range of Ra	σ	Γ	Re_0	γ_{Re}
Current work	10^5–10^8	0.7	1	0.21 ± 0.01	0.518 ± 0.001
Current work	10^5–10^8	0.4	1	0.56 ± 0.01	0.486 ± 0.001
Wagner *et al.* (2012)*	10^4–10^9	0.8	1	0.187	0.496
Emran & Schumacher (2008)*	10^7–10^9	0.7	1	0.33	0.475
Kerr (2001)*	10^6–10^8	0.7	1	—	0.46 ± 0.02
Chavanne *et al.* (2001)	10^7–10^{13}	0.7	1/2	0.271	0.488
Verzicco & Camussi (1999)*	10^4–10^7	0.022	1	—	0.53

TABLE 6. Comparison of Reynolds number scaling as given by (3.3). The asterisk * indicates numerical simulations; the others are experiments.

3.2. *Scaling of Reynolds number with Rayleigh number*

We can also extract the Reynolds number from our velocity field. We calculated the magnitude of the horizontal velocity $\langle v(t) \rangle = \sqrt{u(t)^2 + v(t)^2}$ for both x–z slices ($y = 0$) and y–z slices ($x = 0$). Then we performed an average in the x or y direction, making sure to exclude the sidewall boundary layers, by using an average over the inner 50 % of the cell. We then extracted the maximum $\langle v(t) \rangle$ near the top and bottom plates. Finally, we averaged these $\langle v(t) \rangle$ values over time to obtain $\langle v \rangle$, from which we can determine the Reynolds number

$$Re = \frac{\langle v \rangle}{\sigma}. \tag{3.2}$$

We then plotted the Reynolds number as a function of Rayleigh number in figure 3. We determined the scaling exponent

$$Re = Re_0 Ra^{\gamma_{Re}} \tag{3.3}$$

and included this in table 6 for both Prandtl numbers. We also included results from other groups (if their parameters were similar to ours). We find there is good
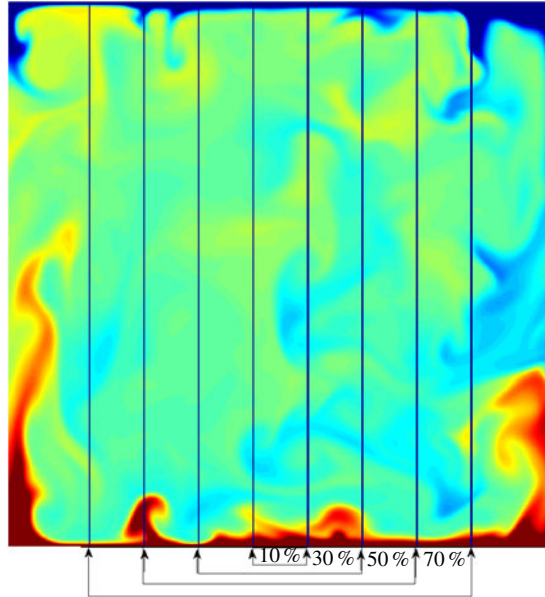
FIGURE 4. (Colour online) A representative example of various cuts (70 to 10 %). The colour density plot is of temperature $\theta(y, z)$ for one snapshot in time, and is for $\sigma = 0.7$, $Ra = 1 \times 10^8$ and a y–z slice ($x = 0$).

agreement. It is expected theoretically (Kraichnan 1962; Grossmann & Lohse 2000) that the scaling exponent should be $1/2$ and our results certainly support this.

3.3. *Scaling of boundary layers with Rayleigh number*

3.3.1. *Calculating boundary layer thicknesses*

After having verified our numerical code in the numerous ways above, we now turn to the main section of the paper, which is a thorough investigation of boundary layers, both viscous and thermal. We need to extract boundary layers from our $\boldsymbol{v}$ and θ data, which are functions of x, y, z and t. For the thermal boundary layers, we find both the temperature $\theta(x, z, t)$ for x–z slices ($y = 0$) and $\theta(y, x, t)$ for y–z slices ($x = 0$). Then we performed an average in the x or y direction to obtain $\theta(z, t)_{len}$. It is unclear as to whether or not an average near the centre of the cell gives the same results as an average over most of the cell (Ahlers *et al.* 2009b; Wagner *et al.* 2012), so we will vary the region over which we average, starting with only 1 % ($len = 1\%$) in the centre and then ramping up to almost all of the cell, but still leaving out the sidewall jets ($len = 70\%$). An example of how we performed these averagings is shown in figure 4. Finally, we averaged these $\langle \theta(z, t) \rangle_{len}$ values over time to obtain $\langle \theta(z) \rangle_{len}$. In addition, there is a difference between finding the instantaneous boundary layer thickness $\lambda_\theta(t)$ for each time slice $\langle \theta(z, t) \rangle_{len}$ and then finding $\langle \lambda_\theta \rangle$ versus finding the boundary layer thickness λ_θ from the time-averaged $\langle \theta(z) \rangle_{len}$.

To add to the mix, one can also define three (or even more) different boundary layer thicknesses (Ahlers *et al.* 2009b): (*a*) λ_θ^{sl} is found from the slope of the thermal profile $\langle \theta(z) \rangle_{len}$ near the top or bottom plate, and then locating the intersection point between this line and mean temperature in the bulk of the cell ($=1$ for our dimensions and rescaling), as shown in figure 5(*a*); (*b*) λ_θ^{95} is found from the distance to 95 % of the bulk temperature (note that in some cases the distance to 99 % of the bulk is used,
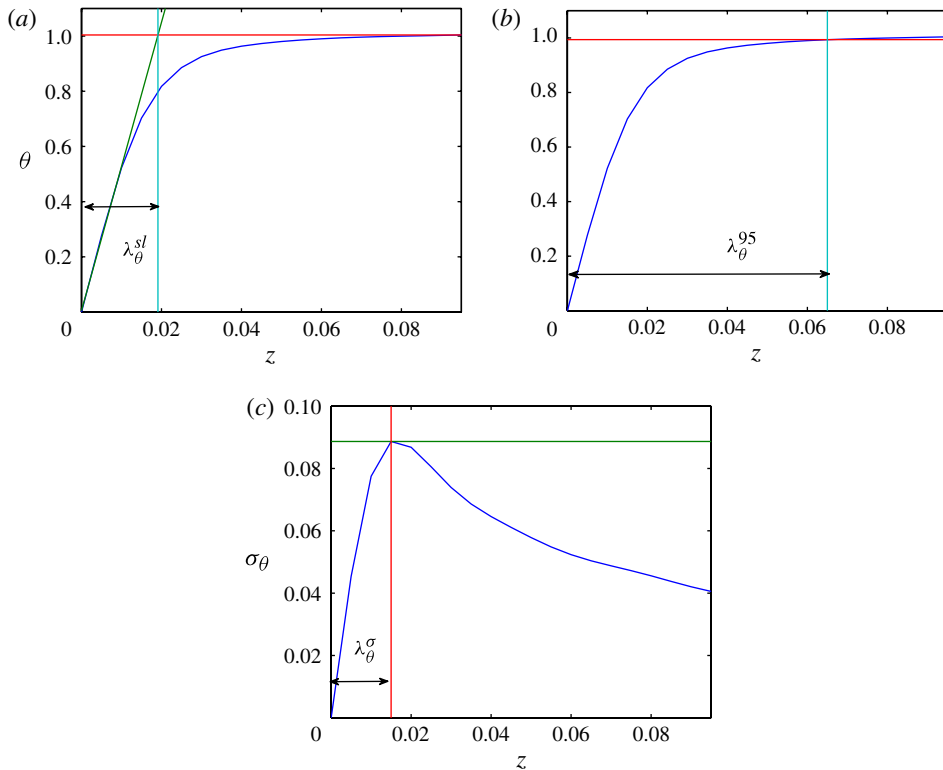
FIGURE 5. (Colour online) Different methods of measuring boundary layer thicknesses: (*a*) the slope method; (*b*) the 95 % from the mean value method; and (*c*) the distance to the maximum of the temperature fluctuation σ_θ, where the temperature fluctuation is found from the standard deviation of $\langle\theta(z)\rangle$.

but for our thermal boundary layer this was not very robust due to the fluctuations in the bulk temperature, so we chose 95 % instead), as shown in figure 5(*b*); and (*c*) λ_θ^σ is found from the distance to the maximal temperature fluctuation, as shown in figure 5(*c*). We computed the maximal temperature fluctuation σ_θ by finding the standard deviation of $\langle\theta(z)\rangle_{len}$. Note that we first performed the averages over x, y and then found the standard deviation of $\langle\theta(z, t)\rangle_{len}$ from our averaged profile $\langle\theta(z)\rangle_{len}$. The viscous boundary layer thicknesses λ_v are found in a similar way for the magnitude of the horizontal velocity $\langle v\rangle$, except that λ_v^{99} is found from the distance to 99 % of the maximum velocity here (99 % worked for this case since the maximum in velocity is very well defined).

We were also careful to be consistent with our slope method of finding boundary layer thickness, since there is a lot of variation in how this value can be computed for different Rayleigh numbers (Wagner *et al.* 2012). For example, we only used the data points in the linear portion of the boundary layer profile, which for our system was defined by the interval $0 < z < 0.005$. If we use a larger z range, the slope can be underestimated, as the boundary layer profile is only linear very near to $z = 0$, especially for higher Rayleigh numbers. Recent experiments (du Puits *et al.* 2012) working at even higher Rayleigh numbers ($\simeq 5 \times 10^{10}$) have found that there is no linear portion for their thermal boundary layer profiles.

We used the mean value of θ in the interval between $0.2 < z < 0.8$ for our bulk temperature to determine the intersection point for λ_θ^{sl}. Our time-averaged bulk temperatures differed from the expected value of 1.0 by at most 1 %. However, these tiny differences can cause the boundary layer thickness to be over- or underestimated. In addition, for the thermal boundary layer thicknesses, we did not rescale our profiles, other than setting the mean value to 1.0, instead of 0.5. This translates into

$$\theta(\text{scaled}) = 2 - 2\theta \quad \text{bottom boundary layer,} \quad (3.4a)$$

$$\theta(\text{scaled}) = 2\theta \quad \text{top boundary layer.} \quad (3.4b)$$

For our viscous boundary layer thickness, we needed to find the maximum velocity v_{max} near the top and bottom boundary layer, since we find the intersection of our linear fit near the boundary with this maximum value. Unfortunately sometimes the instantaneous boundary layer profiles are not so well-behaved (Zhou *et al.* 2010), so finding v_{max} consistently can be problematic. For consistency we set the interval for finding v_{max} to be $0 < z < 0.4$ for the bottom boundary layer and $0.6 < z < 1$ for the top layer. This amounts to finding the global maximum in the bottom and top halves. As investigated by Wagner *et al.* (2012), varying this interval does not seem to make much of a difference. However, we did want to be consistent across Rayleigh numbers, to ensure a robust collapse of the profiles. We did not want to vary our maximum-finding interval with Rayleigh number, which was necessary for a tighter z range near the boundaries, since the location of v_{max} decreases with Rayleigh number.

3.3.2. *Scaling laws*

We are interested in determining the scaling of the boundary layer thicknesses with Rayleigh number, i.e.

$$\lambda_\theta = \lambda_{\theta 0} Ra^{\beta_\theta} \quad (3.5)$$

and

$$\lambda_v = \lambda_{v 0} Ra^{\beta_v}. \quad (3.6)$$

Our scaling results for $\langle \lambda^{sl} \rangle$ for both viscous and thermal boundary layers are given in table 7 along with the results from other groups. The agreement is fairly good with some groups, especially for β_θ.

We compared the scaling results for the various methods of finding boundary layer thicknesses in tables 8 and 9, and representative plots are shown in figures 6 and 7. They are all fairly robust, depending very little on the averaging, in terms of either the cut (70 versus 1 %) or the time averaging ($\langle \lambda^{sl} \rangle$ versus λ^{sl}). The 95–99 % maximum method, λ^{95-99}, consistently gives the smallest exponent. We also found that the exponent for this maximum method approached the value of the exponent for the slope method (λ^{sl}) as the percentage of maximum decreased (from 95 to 80 % for example). We also find that λ^σ tends to give the largest exponent and also the best agreement with the theoretical predictions of Grossmann and Lohse coupled with the laminary boundary layer theory as discussed below.

We also looked at the scaling of the viscous boundary layer thicknesses directly with Reynolds number,

$$\lambda_v = \lambda_{v 0(Re)} Re^{\beta_{v(Re)}}. \quad (3.7)$$

These results are presented in table 10. The results are similar to those in tables 8 and 9, with the best agreement being with the Grossmann–Lohse model for λ^σ, but the other methods all give consistent but different results.

Boundary layers in turbulent RB convection   293

Group	Range of Ra	σ	Γ	$\lambda_{\theta 0}$	β_θ	λ_{u0}	β_v
Current work	10^5–10^8	0.7	1	1.76 ± 0.12	-0.25 ± 0.01	0.40 ± 0.14	-0.18 ± 0.01
Current work	10^5–10^8	0.4	1	1.86 ± 0.16	-0.25 ± 0.01	0.36 ± 0.09	-0.18 ± 0.01
Wagner et al. (2012)*	10^4–10^9	0.8	1	—	-0.285 ± 0.003	—	-0.238 ± 0.009
Stevens, Lohse & Verzicco (2011)*	10^7–10^{12}	0.7	1/2	—	-0.29	—	-0.28
Burnishev et al. (2010)	10^8–10^{12}	0.8	1	4.3 ± 0.3	-0.31 ± 0.02	—	—
Verzicco & Sreenivasan (2008)*	10^6–10^{12}	0.7	1/2	—	$-1/3$	—	—
van Reeuwijk et al. (2008)*	10^5–10^8	1	4	2.33	-0.27	0.5	-0.13
du Puits et al. (2007b)	10^9–10^{12}	0.7	1.13	—	-0.2540	—	—
Verzicco & Camussi (1999)*	10^5–10^8	0.7	1	3.1	-0.29	0.95	-0.23
Belmonte et al. (1994)	10^7–10^{11}	0.7	1	2.5	-0.29	—	—

TABLE 7. Comparison of scaling coefficients from (3.5) and (3.6). Our results are from using a 5 % cut and $\langle \lambda^{sl} \rangle$. Uncertainties are propagated from the standard deviation of the time series of $\lambda^{sl}(t)$. More scaling coefficients are given in table 1. The asterisk * indicates numerical simulations; the others are experiments.

Type	Method	70 %	50 %	30 %	10 %	5 %	1 %
β_θ	λ_θ^{sl}	-0.25	-0.25	-0.26	-0.25	-0.25	-0.25
β_θ	$\langle\lambda_\theta^{sl}\rangle$	-0.26	-0.26	-0.26	-0.25	-0.25	-0.24
β_θ	λ_θ^{95}	-0.19	-0.19	-0.19	-0.19	-0.19	-0.19
β_θ	λ_θ^{σ}	-0.27	-0.28	-0.28	-0.28	-0.28	-0.28
β_v	λ_v^{sl}	-0.18	-0.18	-0.18	-0.18	-0.18	-0.18
β_v	$\langle\lambda_v^{sl}\rangle$	-0.18	-0.18	-0.18	-0.18	-0.18	-0.17
β_v	λ_v^{99}	-0.15	-0.15	-0.15	-0.15	-0.15	-0.15
β_v	λ_v^{σ}	-0.23	-0.24	-0.24	-0.25	-0.25	-0.25

TABLE 8. Scaling exponents β_θ and β_v for $\sigma = 0.7$ and for different cuts (from 70 to 1 %) and different ways of finding the thicknesses as described in the text. In each case the boundary layer values were obtained by finding the thickness for the top and bottom boundary layers for both x and y slices.

Type	Method	70 %	50 %	30 %	10 %	5 %	1 %
β_θ	λ_θ^{sl}	-0.25	-0.26	-0.26	-0.25	-0.25	-0.25
β_θ	$\langle\lambda_\theta^{sl}\rangle$	-0.26	-0.26	-0.26	-0.26	-0.25	-0.24
β_θ	λ_θ^{95}	-0.18	-0.18	-0.18	-0.18	-0.17	-0.17
β_θ	λ_θ^{σ}	-0.26	-0.27	-0.27	-0.27	-0.29	-0.28
β_v	λ_v^{sl}	-0.18	-0.18	-0.19	-0.19	-0.19	-0.19
β_v	$\langle\lambda_v^{sl}\rangle$	-0.19	-0.19	-0.19	-0.19	-0.18	-0.16
β_v	λ_v^{99}	-0.14	-0.14	-0.15	-0.15	-0.15	-0.15
β_v	λ_v^{σ}	-0.18	-0.20	-0.20	-0.21	-0.21	-0.22

TABLE 9. Same as table 8, but for $\sigma = 0.4$

σ	Method	70 %	50 %	30 %	10 %	5 %	1 %
0.7	λ_v^{sl}	-0.34	-0.34	-0.34	-0.34	-0.34	-0.34
0.7	$\langle\lambda_v^{sl}\rangle$	-0.35	-0.35	-0.36	-0.35	-0.34	-0.34
0.7	λ_v^{99}	-0.32	-0.32	-0.32	-0.32	-0.33	-0.33
0.7	λ_v^{σ}	-0.45	-0.45	-0.47	-0.49	-0.48	-0.48
0.4	λ_v^{sl}	-0.37	-0.38	-0.38	-0.39	-0.39	-0.39
0.4	$\langle\lambda_v^{sl}\rangle$	-0.38	-0.39	-0.40	-0.39	-0.37	-0.34
0.4	λ_v^{99}	-0.29	-0.30	-0.30	-0.31	-0.32	-0.32
0.4	λ_v^{σ}	-0.37	-0.41	-0.42	-0.44	-0.44	-0.46

TABLE 10. Same as table 8, but for $\sigma = 0.7$ and $\sigma = 0.4$ and for the scaling exponent $\beta_{v(Re)}$ of the viscous boundary layer thicknesses with Reynolds number instead of Rayleigh number as in (3.7).
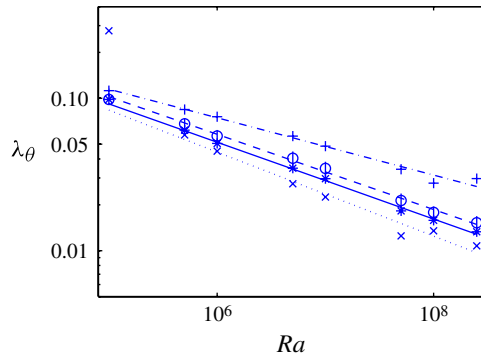
FIGURE 6. (Colour online) Comparison of scaling of thermal boundary layer thicknesses λ_θ with Ra for a representative 5 % cut and different ways of finding the thicknesses, as described in the text: λ_θ^{sl} (solid line, $*$), $\langle\lambda_\theta^{sl}\rangle$ (dashed line, $\circ$), λ_θ^{95} (dashed-dotted line, $+$), and λ_θ^σ (dotted line, $\times$). The scaling exponents are given in table 8. In each case the boundary layer values were obtained by finding the thickness for the top and bottom boundary layers for both x and y slices. Note that $Ra = 1 \times 10^5$ was left out of the fits since it is an outlier. Error bars are given for $\langle\lambda_\theta^{sl}\rangle$ only, since it is the only quantity that varies with time and the uncertainty is found from the standard deviation of the time series.
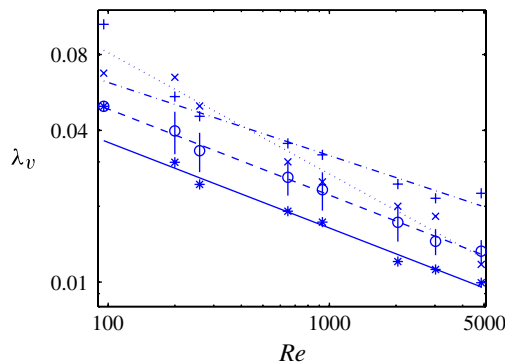
FIGURE 7. (Colour online) Same as figure 6, but for viscous boundary layer thicknesses and scaling with Reynolds number Re instead of Rayleigh number Ra.

Theoretically (Schlichting & Gersten 2000) the boundary layer thicknesses should be

$$\lambda_\theta = \frac{d}{2Nu}, \tag{3.8a}$$

$$\lambda_v = \frac{d}{4\sqrt{Re}}. \tag{3.8b}$$

Our boundary layer scaling results agree fairly well. If we use our scaling results for Nusselt number (table 5) and Reynolds number (table 6), we find for $\sigma = 0.7$ that

$$\frac{\lambda_\theta}{d} = (3.1 \pm 0.8)Ra^{-0.29 \pm 0.01}, \tag{3.9a}$$

$$\frac{\lambda_v}{d} = (0.55 \pm 0.01)Ra^{-0.259 \pm 0.001}, \tag{3.9b}$$

and for $\sigma = 0.4$ that

$$\frac{\lambda_\theta}{d} = (3.1 \pm 0.4)Ra^{-0.284 \pm 0.005}, \tag{3.10a}$$

$$\frac{\lambda_v}{d} = (0.33 \pm 0.01)Ra^{-0.243 \pm 0.001}. \tag{3.10b}$$

Looking at tables 8 and 9, we see that the best agreement in exponent with (3.9) and (3.10) is for λ^σ, but when the uncertainties are taken into account, even the results for λ^{sl} and $\langle\lambda^{sl}\rangle$ in table 7 agree to within two standard deviations (or close to that) except for the exponent β_v. The exponent for λ^{95-99} does not agree as well in all cases. Since the boundary layer thickness is a more local property and the Nusselt number and Reynolds number are global properties, it is not surprising that there is some variation between these quantities.

We find it noteworthy that the viscous boundary layer thickness scales with a consistently lower exponent than the thermal boundary layer thickness for most methods (-0.18 ± 0.01 compared to -0.25 ± 0.01 as in table 7). This is consistent with findings from some groups (Kerr 2001; van Reeuwijk *et al.* 2008; Wagner *et al.* 2012). However, this is in disagreement with the results of Stevens *et al.* (2011), who found the same scaling relation for both the thermal and viscous boundary layers over a wide range of Rayleigh numbers (10^7–10^{12}). However, Stevens used a different definition for the viscous boundary layer thickness, computing the maximum of $\boldsymbol{v} \cdot \nabla^2 \boldsymbol{v}$ instead of the slope of the horizontal velocity as we do here. If one compares our λ_θ^{sl} with λ_v^σ, we do get values for scaling exponents (see table 8) that agree better with one another for $\sigma = 0.7$. However, we think that it is interesting also to compare scaling exponents for the viscous and thermal boundary layer thicknesses obtained from the same methods.

In figure 8 we have plotted $\langle\lambda_v^{sl}\rangle$ and $\langle\lambda_\theta^{sl}\rangle$ together for both $\sigma = 0.7$ and 0.4. Since the viscous boundary layer is thinner than the thermal boundary layer, and it scales with a smaller exponent, a 'cross-over' is expected somewhere between 10^9 and 10^{10} for our Prandtl numbers. It is not clear if there will be a cross-over, or if the scaling exponents will simply change in this range. But it is interesting to note that this is the range where there is significantly more disagreement between theoretical and experimentally or numerically determined boundary layer profiles, at least for $\sigma \simeq 0.7$ (du Puits *et al.* 2009; Stevens *et al.* 2010; Shi *et al.* 2012). It makes sense that there will be disagreement between the theoretical Prandtl–Blasius and the actual curves if λ_v and λ_θ begin to approach one another. The theoretical results (3.11) assume a constant ratio independent of Rayleigh number.
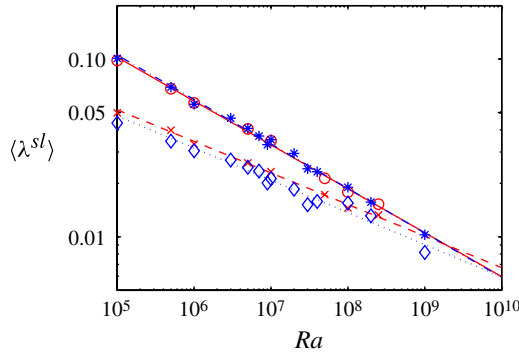
FIGURE 8. (Colour online) Comparison of scaling of boundary layer thicknesses $\langle \lambda^{sl} \rangle$ with Ra for a representative 5 % cut and different Prandtl numbers: $\langle \lambda^{sl}_\theta \rangle$ and $\sigma = 0.7$ (solid line, $\circ$), $\langle \lambda^{sl}_v \rangle$ and $\sigma = 0.7$ (dashed line, $\times$), $\langle \lambda^{sl}_\theta \rangle$ and $\sigma = 0.4$ (dashed-dotted line, $*$), and $\langle \lambda^{sl}_v \rangle$ and $\sigma = 0.4$ (dotted line, $\diamond$). The intersection of $\langle \lambda^{sl}_\theta \rangle$ and $\langle \lambda^{sl}_v \rangle$ for $\sigma = 0.7$ is 2×10^9, and for $\sigma = 0.4$ it is 9×10^9. The error bars were left off this plot for clarity.

3.4. *Boundary layer profiles*

3.4.1. *Theoretical Prandtl–Blasius curves*

The theoretical Prandtl–Blasius solutions (Schlichting & Gersten 2000) are self-similar solutions for the stream function Ψ and the temperature θ:

$$\frac{\mathrm{d}^3\Psi}{\mathrm{d}\xi^3} + 0.5\Psi\frac{\mathrm{d}^2\Psi}{\mathrm{d}\xi^2} = 0, \tag{3.11a}$$

$$\frac{\mathrm{d}^2\theta}{\mathrm{d}\xi^2} + 0.5\sigma\Psi\frac{d\theta}{d\xi} = 0. \tag{3.11b}$$

The initial conditions are given by

$$\Psi(0) = 0, \quad \frac{\mathrm{d}\Psi}{\mathrm{d}\xi}(0) = 0, \quad \frac{\mathrm{d}\Psi}{\mathrm{d}\xi}(\infty) = 1, \tag{3.12a}$$

$$\theta(0) = 0, \quad \theta(\infty) = 1. \tag{3.12b}$$

The horizontal velocity is found from $v = \mathrm{d}\Psi/\mathrm{d}\xi$, and the similarity variable $\xi = z/l$, where l is the length scale, or the boundary layer thickness in this case.

Two points are worth highlighting about the laminar theory. The first is that it is two-dimensional and assumes that the temperature and velocity rise to some constant bulk quantity. The second is that it is a self-similar theory, so boundary layer profiles appropriately scaled with the similarity parameter should all collapse onto the same curve. There is considerable debate (Shi *et al.* 2012; Wagner *et al.* 2012) as to whether the former is a good assumption for three-dimensional RB convection in a cylindrical container where the wind can be wildly varying, in both strength and direction. By averaging over the top and bottom of the container and in the x and y direction, and looking very near the centre of the cell, we have managed to smooth out much of this variation. As a result, we see very good agreement, at least for our viscous boundary layer profiles. However, one of our main interests is in the self-similarity and collapse of the boundary layer profiles, since 'a turbulent boundary layer by definition cannot be universally scaled by outer variables' (van Reeuwijk *et al.* 2008).
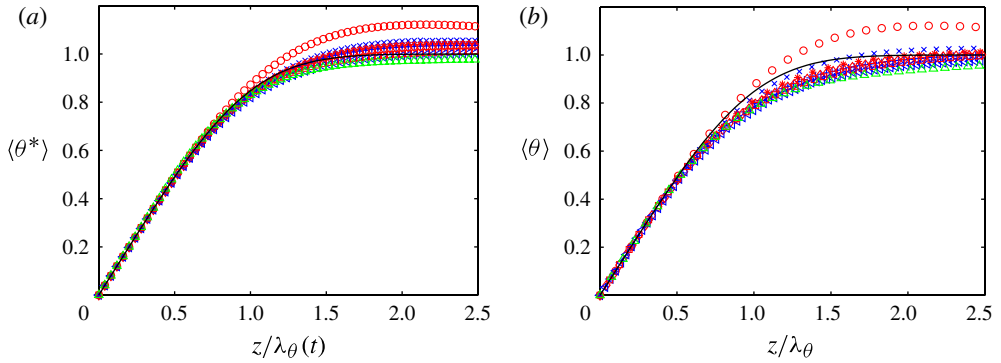
FIGURE 9. (Colour online) Collapse of thermal boundary layer profiles for $\sigma = 0.7$ and a representative 1 % cut, plotted against the theoretical profile (solid line) obtained from solving (3.11). (*a*) Dynamical rescaling, where each $\theta(z, t)$ was scaled by its dynamic boundary layer thickness $\lambda_\theta^{sl}(t)$ and then averaged over time to obtain $\langle \theta^*(z^*) \rangle$. (*b*) Average rescaling, where the average thermal boundary layer $\langle \theta(z) \rangle$ was first computed. Then the z axis was scaled by its boundary layer thickness λ_θ^{sl}. Also, all profiles were rescaled as in (3.4). These plots pertain to an average over x and y slices, and to the top and bottom boundary layers. Corresponding Rayleigh numbers: 1×10^5 (○), 5×10^5 (×), 1×10^6 (∗), 5×10^6 (+), 1×10^7 (◇), 5×10^7 (◁), 1×10^8 (□), and 2.5×10^8 (△).
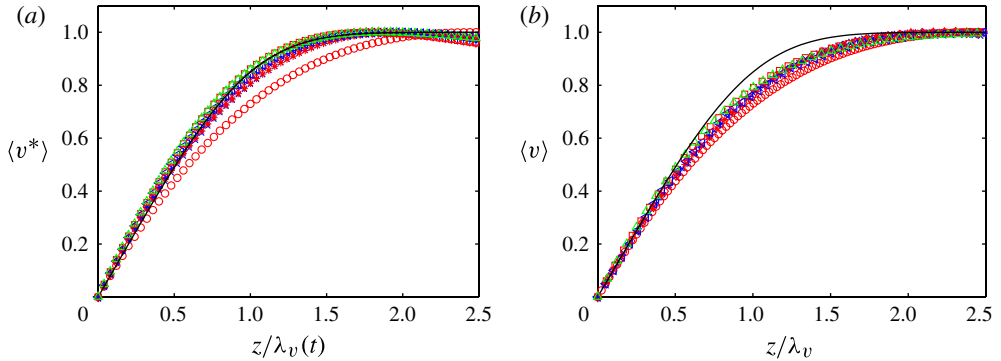
FIGURE 10. (Colour online) Same as figure 9, but for viscous boundary layer thicknesses.

We have plotted a representative set of boundary layer profiles for $\sigma = 0.7$ in figures 9 and 10, and likewise for $\sigma = 0.4$ in figures 11 and 12. In all cases we have used a 1 % cut, which gives the best collapse and agreement with Prandtl–Blasius. For each profile, we also compare the (*a*) dynamic rescaling method introduced by Zhou & Xia (2010) as opposed to (*b*) rescaling after taking the time average of the boundary layer profiles. For the dynamic rescaling method, we scale each of our instantaneous profiles with its respective instantaneous boundary layer thickness, i.e. $z^*(t) = z/\lambda_\theta^{sl}(t)$ for the thermal boundary layer, and $z^*(t) = z/\lambda_v^{sl}(t)$ for the viscous. Then, we find the time-averaged thermal boundary layer profile by performing the
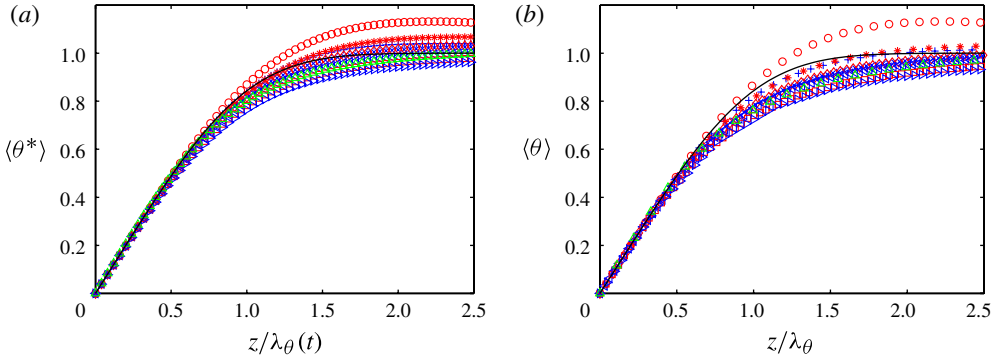
FIGURE 11. (Colour online) Same as figure 9, but for $\sigma = 0.4$. Corresponding Rayleigh numbers: 1×10^5 ($\circ$), 5×10^5 ($\times$), 1×10^6 ($*$), 5×10^6 ($+$), 1×10^7 ($\diamond$), 4×10^7 ($\triangleleft$), 1×10^8 ($\square$), 2×10^8 ($\triangleright$), and 1×10^9 ($\triangle$).
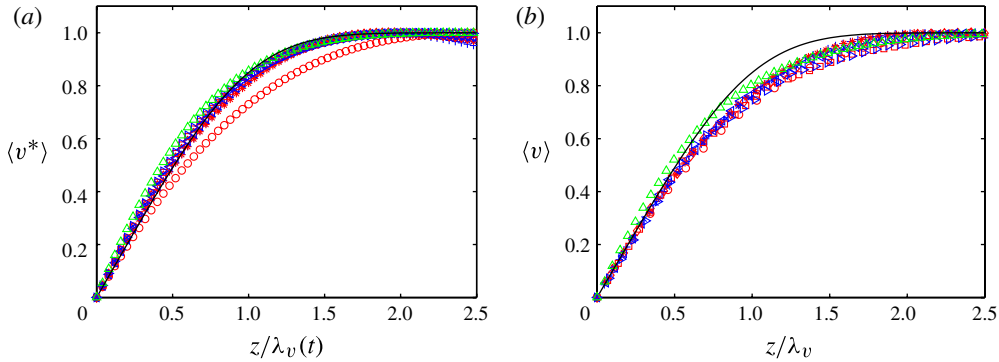
FIGURE 12. (Colour online) Same as figure 11, but for viscous boundary layer thicknesses.

following interpolation:

$$\langle \theta^*(z^*) \rangle = \langle \theta(z, t) \mid z = z^* \lambda_\theta^{sl}(t) \rangle, \tag{3.13a}$$

$$\langle v^*(z^*) \rangle = \langle v(z, t) \mid z = z^* \lambda_v^{sl}(t) \rangle. \tag{3.13b}$$

For the average method, we first find $\langle \theta(z) \rangle$ or $\langle v(z) \rangle$. Then we find the boundary layer thickness associated with those profiles, i.e. λ_θ^{sl} or λ_v^{sl}, and rescale our z axis with these values to obtain a collapse. We find that (for both thermal and viscous boundary layers) the dynamic rescaling always gives better agreement with Prandtl–Blasius than the average method, although collapse is similarly good in both cases.

We have also included the case with a Rayleigh number 1×10^5 in all of our plots for comparison, even though this system is not turbulent. So, when making comparisons to Prandtl–Blasius and collapse of data, please ignore these data. It is interesting, however, that the profile for $Ra = 1 \times 10^5$ is such an outlier, suggesting that the existence of a turbulent state can be gleaned from looking at the shape of the profile. One may even be able to use this shape and the good collapse as a definition of the transition to turbulence.

In general, when looking at the velocity boundary layer profiles in figures 10 and 12, the collapse is very good, and the agreement with the laminar Prandtl–Blasius is quite good for $\sigma = 0.7$ and good for $\sigma = 0.4$, except for the highest Rayleigh number 1×10^9.

However, the thermal boundary layer profiles in figures 9 and 11 do not collapse as well, nor do they agree with the Prandtl–Blasius profile, except for the moderate range of Rayleigh numbers (1×10^6 to 1×10^8). We purposefully did not scale the thermal profiles to unity by dividing by θ_{max}. This was done by Zhou *et al.* (2011), and much better agreement with Prandtl–Blasius is obtained then. However, the temperature profiles all rise from zero at the plate to one in the bulk, so no rescaling is required. In contrast, for the viscous profiles, whose maximum velocity increases with Rayleigh number, one needs to rescale with v_{max} to test collapse. Hence, minor differences in thermal boundary layer profiles are highlighted here. We think that they are important and suggest that the thermal boundary layer profiles do not collapse all that well, and also do not follow the Prandtl–Blasius shape very well.

3.4.2. *Shape factors*

We can be more quantitative about our boundary layer profiles by computing shape factors (Zhou & Xia 2010). For our viscous boundary layer profiles, the shape factor is a ratio of two quantities, the displacement thickness

$$\delta_d = \int_0^\infty \left(1 - \frac{v(z)}{[v(z)]_{max}} \right) \, \mathrm{d}z, \tag{3.14}$$

and the momentum thickness

$$\delta_m = \int_0^\infty \left(1 - \frac{v(z)}{[v(z)]_{max}} \right) \left(\frac{v(z)}{[v(z)]_{max}} \right) \, \mathrm{d}z. \tag{3.15}$$

The shape factor for the viscous boundary layer is then

$$S_v = \frac{\delta_d}{\delta_m}, \tag{3.16}$$

and S_v is found to be 2.59 for the theoretical Prandtl–Blasius curve.

An analogous shape factor S_θ can be defined for the thermal boundary layer, where $v(z)$ is replaced by $\theta(z)$ in (3.14)–(3.16). Since the measured thermal boundary layers can either over- or undershoot their mean bulk value as they rise and level off (see figure 9), it is difficult to define a θ_{max} consistently in the analogous thermal equations. In the case of undershoot, the value for θ_{max} also becomes dependent on the interval chosen for integration. For consistency, we used the computed mean bulk value in each case for θ_{max}. We also chose the same interval to integrate over for each case. The thermal shape factor computed for the theoretical Prandtl–Blasius profiles is dependent on Prandtl number, and $S_\theta = 2.58$ for $\sigma = 0.7$ and $S_\theta = 2.56$ for $\sigma = 0.4$. If our computed shape factors are less than the Prandtl–Blasius values, this indicates that the curve rises more slowly, and vice versa (Zhou *et al.* 2010).

As a way of synthesizing all of the information about boundary layer profiles, we have plotted the shape factors for $\sigma = 0.7$ in figure 13 and for $\sigma = 0.4$ in figure 14. In both figures, the top row corresponds to the dynamic rescaling method and the bottom row corresponds to the average method. We can clearly see that the best collapse and agreement with Prandtl–Blasius is for the dynamic rescaling method and for a 1 % cut down the middle of the cell. Even then, one can see that the highest Rayleigh numbers (as green triangles, $\triangle$) tend to fall the lowest below the Prandtl–Blasius
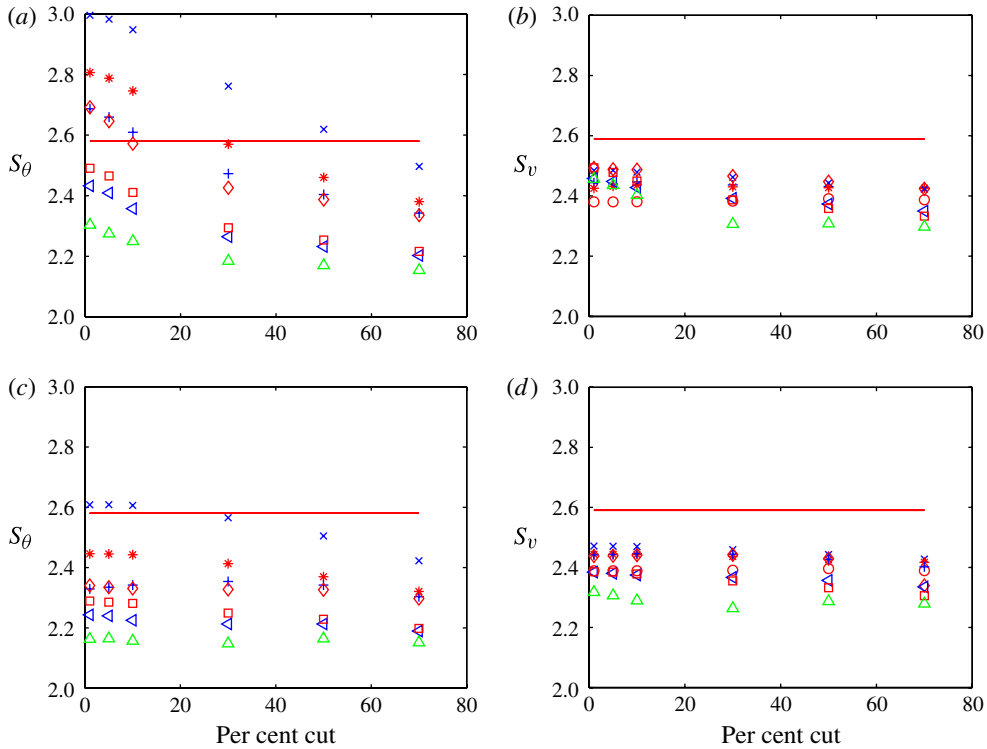
FIGURE 13. (Colour online) Shape factors as defined by (3.16) for $\sigma = 0.7$ and $\Gamma = 1$ for various averagings (1, 5, 10, 30, 50, 70 %). The solid line is the shape factor for the theoretical Prandtl–Blasius curve. (*a*) Shape factors found from profiles of thermal boundary layers averaged via the dynamic rescaling method. (*b*) Shape factors found from profiles of viscous boundary layers averaged via the dynamic rescaling method. (*c*) Shape factors found from time-averaged profiles of thermal boundary layers. (*d*) Shape factors found from time-averaged profiles of viscous boundary layers. Corresponding Rayleigh numbers: 1×10^5 (○), 5×10^5 (×), 1×10^6 (∗), 5×10^6 (+), 1×10^7 (◇), 5×10^7 (◁), 1×10^8 (□), and 2.5×10^8 (△).

curve, suggesting an increasing disagreement as Rayleigh number increases. Please ignore the red circles, which are for $Ra = 1 \times 10^5$, which is not turbulent and so is expected to be an outlier (and does not even fall on the correct scale for some of our S_θ values).

There are a few details about our method of finding boundary layer profiles that should be mentioned here. First of all, we do not find our local boundary layer thickness as a function of r, the radial distance from the centre of the cell. Instead, we first obtain the horizontally averaged $\langle \theta (z, t) \rangle_{len}$ and then compute the local boundary layer thickness from this value. Hence our 1 and 5 % results give better 'locally' averaged results if the boundary layer thickness varies with r as found in Zhou *et al.* (2011) and Wagner *et al.* (2012). Owing to the overall noisiness of the large-scale circulation (LSC) for fully three-dimensional systems, any azimuthal average will not extract the radial dependence of local boundary layer thicknesses any more correctly than our horizontal averaging. It would be interesting, however, to extend our local
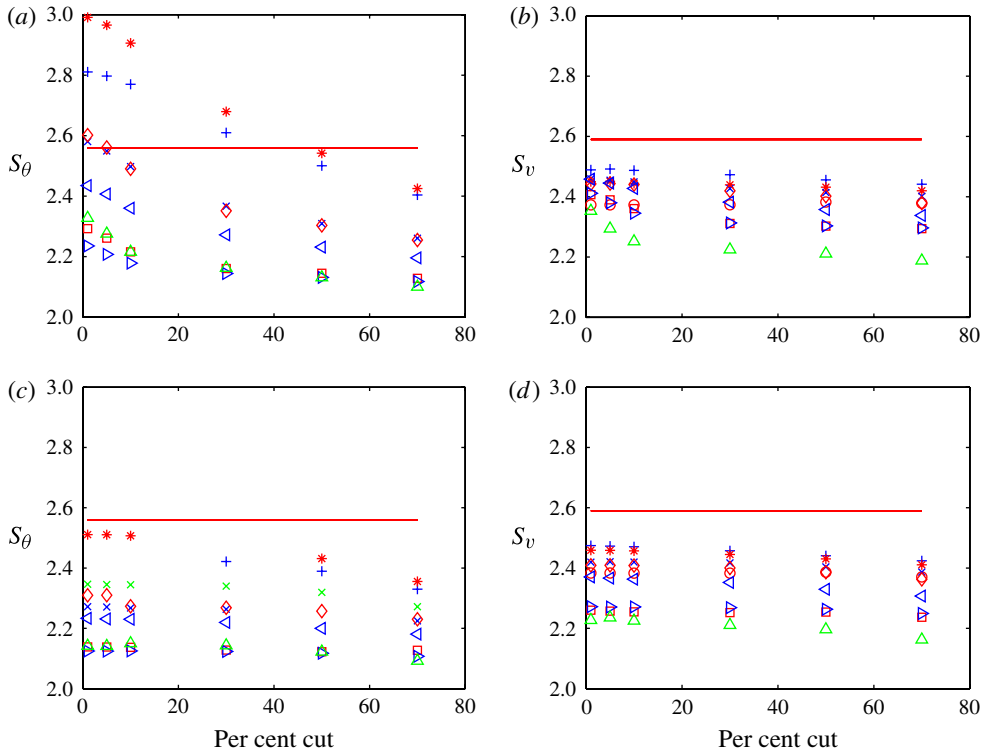
FIGURE 14. (Colour online) Same as figure 13, but for $\sigma = 0.4$. Corresponding Rayleigh numbers: 1×10^5 ($\circ$), 5×10^5 ($\times$), 1×10^6 ($*$), 5×10^6 ($+$), 1×10^7 ($\diamond$), 4×10^7 ($\triangleleft$), 1×10^8 ($\square$), 2×10^8 ($\triangleright$), and 1×10^9 ($\triangle$).

analysis near the centre of the cell (1 %) to other locations as is done in Wagner *et al.* (2012). This is something we plan to investigate in the future.

We also did not take the direction of the LSC into account, as has been done by Shi *et al.* (2012) and Wagner *et al.* (2012). Again, owing to the drift, sloshing, torsional modes of the LSC, it is rather difficult to extract the direction of the LSC, except instantaneously or for very short time intervals over which the LSC is stable. Again, this makes our analysis near the centre of the cell the best for comparison when considering the orientation of the LSC. Since others have found the boundary layer in relation to the LSC, our analysis done in a different manner makes for a nice comparison.

The overall conclusion is that a small window near the centre is the best 'local' boundary layer analysis, and this is supported by our results. We see in figures 13 and 14 that the differences between the dynamical rescaling and the average method become less pronounced as more of the cell is included in the average (1 versus 70 %). This is because our dynamical method becomes less 'local' as we perform an average over more of the horizontal extent of the cell. It is also because the averaging smooths out the fluctuations (to some extent) and so the shape factors collapse better, independently of method. The agreement with the Prandtl–Blasius profile is still better for the dynamical rescaling method than the average method independent of percentage cut.

4. Conclusion

In conclusion, we find that the boundary layer profiles can give significant insight into the state of the system. For example, the profiles for non-turbulent RB convection ($Ra = 1 \times 10^5$ for our Prandtl numbers of 0.7 and 0.4) have a different shape than those for a fully turbulent RB convection case. For moderate Rayleigh numbers ($1 \times 10^6 < Ra < 1 \times 10^8$), the profiles tend to collapse well, and follow the Prandtl–Blasius shape, especially for our viscous boundary layer profiles, suggesting a typical laminar profile and a well-developed large-scale circulation. Our thermal boundary layer profiles do not collapse as well and do not agree as well with the Prandtl–Blasius shape. Even for the viscous boundary layer profiles, we see a very slight disagreement with collapse and Prandtl–Blasius shape for our highest Rayleigh numbers, suggesting that the trend is to disagree for even higher Rayleigh numbers, consistent with the results of others. The fact that the thermal and viscous boundary layer thicknesses also start to approach one another at the same time as in figure 8 further supports a deviation from the Prandtl–Blasius theory.

We find that the scaling of boundary layer thicknesses is fairly robust, and independent of the method (dynamical versus average) and amount of spatial averaging. This is consistent with the results of Zhou & Xia (2010). Our results mostly agree with the laminar boundary layer theory coupled with the Grossmann and Lohse theory scaling when numerical uncertainties are taken into account. The fluctuation method λ^σ (the boundary layer thickness found from the distance to the maximal fluctuation of the boundary layer) gives the best agreement.

Note that we looked at the x and y slices as well as the top and bottom boundary layers independently to see if there was any asymmetry, but did not find any discernible trends; hence in all cases we averaged our data over both x and y slices as well as top and bottom layers.

We plan to perform simulations at even higher Rayleigh numbers to see if our trends continue, and to better understand the deviation from Prandtl–Blasius theory that is seen by other groups in this regime. We also plan to investigate the LSC more fully in future work. Other groups (Maystrenko, Resagk & Thess 2007; Shi *et al.* 2012; Wagner *et al.* 2012) have looked at boundary layer profiles in the direction of the mean wind, and they have found more disagreement with Prandtl–Blasius. However, they also looked at higher Rayleigh number, so it would be interesting to determine if the deviations at higher Rayleigh number are intrinsic to RB convection at $\sigma = 0.7$, or if it is a function of how the boundary layers are extracted.

REFERENCES

AHLERS, G., BODENSCHATZ, E., FUNFSCHILLING, D. & HOGG, J. 2009*a* Turbulent Rayleigh–Bénard convection for a Prandtl number of 0.67. *J. Fluid Mech.* **641**, 157–167.

AHLERS, G., GROSSMANN, S. & LOHSE, D. 2009*b* Heat transfer and large-scale dynamics in turbulent Rayleigh–Bénard convection. *Rev. Mod. Phys.* **81**.

BAILON-CUBA, J., EMRAN, M. S. & SCHUMACHER, J. 2010 Aspect ratio dependence of heat transfer and large-scale flow in turbulent convection. *J. Fluid Mech.* **655**, 152–173.

BELMONTE, A., TILGNER, A. & LIBCHABER, A. 1994 Temperature and velocity boundary layers in turbulent convection. *Phys. Rev.* E **50**, 269–279.

BENZI, R., TOSCHI, F. & TRIPICCIONE, R. 1998 On the heat transfer in Rayleigh–Bénard systems. *J. Stat. Phys.* **93**, 901–918.

BREUER, M., WESSLING, S., SCHMALZL, J. & HANSEN, U. 2004 Effect of inertia in Rayleigh–Bénard convection. *Phys. Rev.* E **69**, 026302.

BROWN, E., NIKOLAENKO, A. & AHLERS, G. 2005 Reorientation of the large-scale circulation in turbulent Rayleigh–Bénard convection. *Phys. Rev. Lett.* **95**, 084503.

BURNISHEV, Y., SEGRE, E. & STEINBERG, V. 2010 Strong symmetrical non-Oberbeck–Boussinesq turbulent convection and the role of compressibility. *Phys. Fluids* **22**, 035108.

CASTAING, B., GUNARATNE, G., HESLOT, F., KADANOFF, L., LIBCHABER, A., THOMAE, S., WU, X.-Z., ZALESKI, S. & ZANETTI, G. 1989 Scaling of hard thermal turbulence in Rayleigh–Bénard convection. *J. Fluid Mech.* **204**, 1–30.

CHANDRA, M. & VERMA, M. K. 2011 Dynamics and symmetries of flow reversals in turbulent convection. *Phys. Rev.* E 067303.

CHANDRASEKHAR, S. 1961 *Hydrodynamic and Hydromagnetic Stability*. Oxford University Press.

CHAVANNE, X., CHILLA, F., CASTAING, B., HEBRAL, B., CHABAUD, B. & CHAUSSY, J. 1997 Observation of the ultimate regime in Rayleigh–Bénard convection. *Phys. Rev. Lett.* **79**, 3648–3651.

CHAVANNE, X., CHILLA, F., CASTAING, B., HEBRAL, B., CHABAUD, B. & CHAUSSY, J. 2001 Turbulent Rayleigh–Bénard convection in gaseous and liquid He. *Phys. Fluids* **13**, 1300–1320.

EMRAN, M. S. & SCHUMACHER, J. 2008 Finite-scale statistics of temperature and its derivatives in convective turbulence. *J. Fluid Mech.* **611**, 13–34.

FISCHER, P. F., LOTTES, J. W. & KERKEMEIER, S. G. 2008 nek5000 web page (http://nek5000.mcs.anl.gov).

FUNFSCHILLING, D. & AHLERS, G. 2004 Plume motion and large-scale circulation in a cylindrical Rayleigh–Bénard cell. *Phys. Rev. Lett.* **92**, 194502.

FUNFSCHILLING, D., BODENSCHATZ, E. & AHLERS, G. 2009 Search for the ultimate state in turbulent Rayleigh–Bénard convection. *Phys. Rev. Lett.* **103**, 014503.

GROSSMANN, S. & LOHSE, D. 2000 Scaling in thermal convection: a unifying theory. *J. Fluid Mech.* **407**, 27–56.

HE, X., FUNFSCHILLING, D., NOBACH, H., BODENSCHATZ, E. & AHLERS, G. 2012 Transition to the ultimate state of turbulent Rayleigh–Bénard convection. *Phys. Rev. Lett* **108**, 024502.

KERR, R. M. 2001 Energy budget in Rayleigh–Bénard convection. *Phys. Rev. Lett.* **87**, 244502.

KRAICHNAN, R. H. 1962 Turbulent thermal convection at arbitrary Prandtl number. *Phys. Fluids* **5**, 1374–1389.

LAM, S., SHANG, X.-D., ZHOU, S.-Q. & XIA, K.-Q. 2002 Prandtl number dependence of the viscous boundary layer and the Reynolds numbers in Rayleigh–Bénard convection. *Phys. Rev.* E **65**, 066306.

LUI, S.-L. & XIA, K.-Q. 1998 Spatial structure of the thermal boundary layer in turbulent convection. *Phys. Rev.* E **57**, 5494–5503.

MAYSTRENKO, A., RESAGK, C. & THESS, A. 2007 Structure of the thermal boundary layer for turbulent Rayleigh–Bénard convection of air in a long rectangular enclosure. *Phys. Rev.* E **75**, 066303.

NIEMELA, J. J., SKRBEK, L., SREENIVASAN, K. R. & DONNELLEY, R. J. 2000 Turbulent convection at very high Rayleigh numbers. *Nature* **404**, 837–840.

DU PUITS, R., RESAGK, C. & THESS, A. 2007*a* Mean velocity profile in confined turbulent convection. *Phys. Rev. Lett.* **99**, 234504.

DU PUITS, R., RESAGK, C. & THESS, A. 2009 Structure of viscous boundary layers in turbulent Rayleigh–Bénard convection. *Phys. Rev.* E **80**, 036318.

du Puits, R., Resagk, C. & Thess, A. 2010 Thickness of the diffusive sublayer in turbulent convection. *Phys. Rev.* E **81**, 016307.

du Puits, R., Resagk, C. & Thess, A. 2012 Thermal boundary layers in turbulent Rayleigh–Bénard convection at aspect ratio between 1 and 9. *New J. Phys.* (submitted).

du Puits, R., Resagk, C., Tilgner, A., Busse, F. H. & Thess, A. 2007*b* Structure of thermal boundary layers in turbulent Rayleigh–Bénard convection. *J. Fluid Mech.* **572**, 231–254.

Qiu, X.-L. & Xia, K.-Q. 1998 Spatial structure of the viscous boundary layer in turbulent convection. *Phys. Rev.* E **58**, 5816–5820.

van Reeuwijk, M., Jonker, H. J. J. & Hanjalic, K. 2008 Wind and boundary layers in Rayleigh–Bénard convection. II. Boundary layer character and scaling. *Phys. Rev.* E **77**, 036312.

Schlichting, H. & Gersten, K. 2000 *Boundary Layer Theory*, 8th edn. Springer.

Shi, N., Emran, M. S. & Schumacher, J. 2012 Boundary layer structure in turbulent Rayleigh–Bénard convection. *J. Fluid Mech.* **706**, 5–33.

Shishkina, O., Stevens, R. J. A. M., Grossmann, S. & Lohse, D. 2010 Boundary layer structure in turbulent thermal convection and its consequences for the required numerical resolution. *New J. Phys.* **12**, 075022.

Shishkina, O. & Thess, A. 2009 Mean temperature profiles in turbulent Rayleigh–Bénard convection of water. *J. Fluid Mech.* **633**, 449–460.

Sreenivasan, K. R., Bershadskii, A. & Niemela, J. J. 2002 Mean wind and its reversal in thermal convection. *Phys. Rev.* E **65**, 056306.

Stevens, R. J. A. M., Lohse, D. & Verzicco, R. 2011 Prandtl and Rayleigh number dependence of heat transport in high Rayleigh number thermal convection. *J. Fluid Mech.* **688**, 31–43.

Stevens, R. J. A. M., Verzicco, R. & Lohse, D. 2010 Radial boundary layer structure and Nusselt number in Rayleigh–Bénard convection. *J. Fluid Mech.* **643**, 495–507.

Stevens, R. J. A. M., Zhou, Q., Grossmann, S., Verzicco, R., Xia, K.-Q. & Lohse, D. 2012 Thermal boundary layer profiles in turbulent Rayleigh–Bénard convection in a cylindrical sample. *Phys. Rev.* E 027301.

Sun, C., Cheung, Y.-H. & Xia, K.-Q. 2008 Experimental studies of the viscous boundary layer properties in turbulent Rayleigh–Bénard convection. *J. Fluid Mech.* **605**, 79–113.

Urban, P., Musilova, V. & Skrbek, L. 2011 Efficiency of heat transfer in turbulent Rayleigh–Bénard convection. *Phys. Rev. Lett.* **107**, 014302.

Verzicco, R. & Camussi, R. 1999 Prandtl number effects in convective turbulence. *J. Fluid Mech.* **383**, 55–73.

Verzicco, R. & Camussi, R. 2003 Numerical experiments on strongly turbulent thermal convection in a slender cylindrical cell. *J. Fluid Mech.* **477**, 19–49.

Verzicco, R. & Sreenivasan, K. R. 2008 A comparison of turbulent thermal convection between conditions of constant temperature and constant heat flux. *J. Fluid Mech.* **595**, 203–219.

Wagner, S., Shishkina, O. & Wagner, C. 2012 Boundary layers and wind in cylindrical Rayleigh–Bénard cells. *J Fluid Mech.* **607**, 336.

Wu, X.-Z. & Libchaber, A. 1992 Scaling relations in thermal turbulence: the aspect-ratio dependence. *Phys. Rev.* A **45**, 842–845.

Xin, Y.-B., Xia, K.-Q. & Tong, P. 1996 Measured velocity boundary layers in turbulent convection. *Phys. Rev. Lett.* **77**, 1266–1269.

Zhou, Q., Stevens, R. J. A. M., Sugiyama, K., Grossmann, S., Lohse, D. & Xia, K.-Q. 2010 Prandtl–Blasius temperature and velocity boundary-layer profiles in turbulent Rayleigh–Bénard convection. *J. Fluid Mech.* **664**, 297–312.

Zhou, Q., Sugiyama, K., Stevens, R. J. A. M., Grossmann, S., Lohse, D. & Xia, K.-Q. 2011 Horizontal structures of velocity and temperature boundary-layer profiles in 2D numerical turbulent Rayleigh–Bénard convection. *Phys. Fluids* **23**, 125104.

Zhou, Q., Sun, C. & Xia, K.-Q. 2007 Morphological evolution of thermal plumes in turbulent Rayleigh–Bénard convection. *Phys. Rev. Lett.* **98**, 074501.

Zhou, Q. & Xia, K.-Q. 2010 Measured instantaneous viscous boundary layer in turbulent Rayleigh–Bénard convection. *Phys. Rev. Lett.* **104**, 104301.